Article

Discovery Medicine 2026; 38(206): 906–920
https://doi.org/10.24976/Discov.Med.202638206.74

Rapid Label-free SERS Detection of Viruses Using Bistratal Hydrogel Film@Au Nanoparticles Arrays

Yanchun Li[1,2], Yamin Chai[2], Zuoliang Dong[2], Zhixian Gao[1,*]

[1]Tianjin Key Laboratory of Risk Assessment and Control Technology for Environment and Food Safety, Military Medical Sciences Academy, Academy of Military Sciences, 300050 Tianjin, China
[2]Laboratory Medicine Center, Tianjin Medical University General Hospital, 300052 Tianjin, China
*Correspondence: gaozhx@163.com (Zhixian Gao)
Submitted: 26 September 2025 Revised: 6 February 2026 Accepted: 27 February 2026 Published: 20 March 2026

Background: Due to their unpredictable and variable nature, novel viruses pose a significant threat to human health as well as to the economy and society. Rapid detection plays a crucial role in the surveillance and management of the transmission and emergence of novel viruses. This study aims to establish a rapid, label-free surface-enhanced Raman scattering (SERS) platform for the highly sensitive and specific identification of emerging viruses.
Methods: A novel self-assembly strategy based on the synergistic effect of electrostatic adsorption and hydrogel contraction has been developed to construct highly ordered hexagonally close-packed Au nanoparticle arrays on both surfaces of a polyacrylamide composite hydrogel film. The drying and shrinking of the hydrogel film contribute to the reduction of the particle gap, facilitating the formation of "hot spots" that effectively enhance near-field coupling and significantly amplify the local electromagnetic field in its vicinity. The label-free SERS detection of viruses relies on the intrinsic Raman fingerprints of viral structural components, particularly the envelope glycoproteins and lipid membranes that differ distinctly from host cellular materials.
Results: The detection of malachite green and crystal violet on the substrate indicates high Raman optical activity. Validation with probe molecules (crystal violet, malachite green) showed low limits of detection (LOD of 10^{-11} M) and high linearity ($R^2 >$ 0.996). Highly linear quantitative sensitivity was observed, with a limit of detection of 1 TU/mL for both severe acute respiratory syndrome coronavirus 2 (SARS-CoV-2) Spike pseudovirus and B6R Mpox pseudovirus.
Conclusion: The composite material is anticipated to serve as a novel Raman substrate, enabling the rapid identification of novel viruses and facilitating a prompt response to epidemics.

Keywords: surface-enhanced Raman spectroscopy; hot spots; SARS-CoV-2; Mpox

Introduction

Novel viruses, unknown and unpredictable, pose significant threats to human health, the economy, and the environment. The highly contagious coronavirus disease 2019 (COVID-19) pandemic, caused by severe acute respiratory syndrome coronavirus 2 (SARS-CoV-2), has prompted a global public health emergency. SARS-CoV-2 is an enveloped, positive-sense, single-stranded ribonucleic acid (RNA) virus with a 30-kb genome that encodes for four structural proteins spike (S), envelope (E), membrane (M), nucleocapsid (N), non-structural proteins (nsp1-nsp16), and putative accessory proteins [1]. The World Health Organization (WHO) reports that by the end of 2024, there have been 777,310,393 confirmed cases of COVID-19, along with 7,083,246 deaths and a fatality rate of approximately 0.911% (https://covid19.who.int/). The emergence of novel coronavirus varieties presents ongoing problems for public health and the control of epidemics concomitantly. Moreover, the ongoing Monkeypox virus (Mpox) pandemic has also emerged as another major public health concern and has drawn considerable attention from the medical community. Mpox is a zoonotic double-stranded DNA (dsDNA) orthopoxvirus that encodes 181 proteins and produces two types of infectious virions: the intracellular mature virus and the extracellular enveloped virus [2]. It can be transmitted to humans through physical contact with an infected individual, exposure to contaminated materials, or contact with infected animals. Typical manifestations of mpox include a rash or mucosal lesions that can persist for two to four weeks, along with fever, headache, myalgia, back discomfort, low energy, and enlarged lymph nodes [3]. The global outbreak has been attributed to clade IIb (West African clade) of Mpox. From 01 January 2022 to 30 November 2024, a total of 117,663 laboratory-confirmed cases, including 185 deaths, were reported to the WHO (https://worldhealthorg.shinyapps.io/mpx_global/). The primary objective of surveillance, case investigation, and contact tracing is to promptly identify new outbreaks and interrupt human-to-human transmission in order to effectively control the global epidemic and minimize zoonotic spread.

Diagnostic testing methods for viruses mainly include nucleic acid amplification tests (NAATs), antigen, antibody detections, or in combination with genomic sequencing. Standard confirmation of SARS-CoV-2 and Mpox infections is based on the detection of unique viral sequences by nucleic acid amplification tests in appropriately equipped laboratory-based conditions. Primers and probes approved for SARS-CoV-2 are designed as a two-target system for target genes of *ORF1ab*, *E*, *N* or *RdRp* [4]. For Mpox, the conserved regions of the core coding sequence are the focus of published primers and probes, such as E9L-NVAR in the DNA polymerase gene, B6R in the envelope protein gene, and F3L in the ORF [5]. The integration of CRISPR/cas12a-mediated technology with lateral flow assay (LFA) readout has shown promising potential in transforming this technique into a genuine point-of-care test (POCT) [6–8]. Furthermore, rapid diagnostic tests (RDTs), such as Ag- or Ab- detecting diagnostic assays, have been performed in the format of LFA or immunofluorescence (IFA) to directly identify some kinds of viral proteins. Despites potential benefits of POCT, LFA for SARS-CoV-2 detection has shown lower sensitivity and specificity inferior to the PCR assays, and relative to the method of sample collection and infection periods [9–11]. However, serological testing for antibodies or antigens for Mpox detection has not been extensively adopted. The current state of diagnostic technology still presents gaps that need to be addressed in order to enable rapid detection and prompt response to emerging virus outbreaks.

Owing to its superior sensitivity, capability for multiplex detection, and non-destructive nature compared to traditional methods, surface-enhanced Raman spectroscopy (SERS) provides a promising platform for rapid detection. The electromagnetic (EM) enhancement and the chemical enhancement both contribute to the amplification of SERS, while the EM mechanism accounts for the majority of the increase by a factor of $\sim 10^6$ [12]. The magnitude of signal enhancement is primarily determined by several key factors, including the martials, the hot spots and the analyte-surface distance [13]. Gold-based nanostructures or gold nanoparticles (Au NPs) are mostly used for biosensing applications due to their biocompatibility, tunability, uniformity and electronic properties. Different colloidal active Au NPs shapes, such as nanospheres, cubes, plates, rods, nanoprisms and stars, have been proposed and demonstrated for an enhancement factor (EF) ranging from 10^5 to 10^{10} of various SERS active molecules [14]. In addition, the EF can be effectively increased by synergistically controlling hot spots in gold nanoparticles, producing a re-enhancement effect. The strategies include interparticle coupling, particle-substrate coupling and multilayer substrates [15–18]. Though electron-beam lithography, focused-ion beam milling, and nanoimprint lithography have been used to fabricate reproducible and scalable SERS substrates, these lithography-based technologies are time-consuming and require high-cost infrastructure. Whereas, the utilization of nanoparticles self-assembly based on template-assisted [19–21], evaporation [22–24], and interficial assembly [25,26] allows for the simple and cost-effective fabrication of thin-film SERS substrates.

The label-free SERS detection of viruses relies on the intrinsic Raman fingerprints of viral structural components, particularly the envelope glycoproteins and lipid membranes that differ distinctly from host cellular materials. Non-enveloped viruses possess icosahedral or helical capsids composed of repeating protein subunits capsomeres that offer abundant Raman-active targets. This study presents a novel enhanced substrate for the rapid label-free SERS detection of SARS-CoV-2 and Mpox. In this study, we employ the self-assembly method of Au NPs electrostatically absorbed onto hydrogels to facilitate rapid SERS detection of SARS-CoV-2 and Mpox by generating localized hot spots with uniform particle sizes. The desiccation and contraction of hydrogel, localized surface plasmon resonance (LSPR) of interparticle and interlayer, is improved, which is beneficial for achieving higher sensitivity Raman detection of novel viruses based on hot spots.

Materials and Methods

Reagents and Materials

Gold (III) chloride hydrate ($HAuCl_4 \cdot 3H_2O$, 99.9%: Aladdin, Cat. No. 16961-25-4), acrylamide (AAm, ≥99.9%: Aladdin, Cat. No.9003-05-8), acrylic acid (AAc, ≥99.9%: Aladdin, Cat. No. 79-10-7), poly(diallyldimethylammonium chloride) solution (PDADMAC, 20 wt.% in H_2O: Aladdin, Cat. No.26062-79-3) and 2-Hydroxy-4′-(2-hydroxyethoxy)-2-methylpropiophenone (Irgacure 2959, ≥98%: Aladdin, Cat. No. 106797-53-9) were purchased from Aladdin Industrial Corporation. Dimethyl sulfoxide (DMSO, 99.5%: Sinopharm, Cat. No. 67-68-5), N,N′-Methylenebisacrylamide (MBAAm, ≥97%, Cat. No. 110-26-9), Ethylene glycol (≥99.5%, Sinopharm, Cat. No. 110-26-9), crystal violet (CV, Sinopharm, Cat. No. 548-62-9) and malachite green (MG, Sinopharm, Cat. No. 569-64-2) were purchased from Sinopharm Reagent Co., Ltd. SARS-CoV-2 Spike Protein Pseudovirus (Cat. No. 11906ES50) and Mpox B6R Pseudovirus (Cat. No. 12100ES03) were purchased by Yeasen Biotechnology (Shanghai) Co., Ltd. Deionized water with a conductivity of less than 0.1 us/cm and an electrical resistivity greater than or equal to 10 MΩ·cm was purchased from Guangdong Qianjing Corporation. All reagents were used as received without further purification.

Clinical samples from July 2024 to March 2025 were obtained after approval from the Medical Ethics Committee of Tianjin Medical University General Hospital (IRB approval number: 2025-KY-533) and in strict adherence to the principle of informed consent and the Declaration of

Helsinki. A total of 20 nasopharyngeal swabs positive for SARS-CoV-2 and 10 skin swabs positive for Mpox, as confirmed by standard diagnostic methods (RT-PCR for SARS-CoV-2 and PCR for Mpox), were initially placed into sterile containers with viral transport medium. In addition, 10 negative samples of SARS-CoV-2 and monkeypox virus were selected as negative controls. The samples were then vortexed for 30 seconds to release viral particles, followed by centrifugation at 10,000 rpm for 5 minutes to remove cellular debris. The resulting supernatant, containing viral particles, was collected and stored at –80 °C until analysis. Prior to SERS analysis, samples were thawed at 4 °C, and 1 µL of the diluted sample was applied onto the hydrogel@Au NPs substrate and air-dried.

Instruments

Surface morphology was characterized using an atomic force microscope Dimension Icon (Bruker Corporation, Santa Barbara, CA, USA) in tapping mode. The scanning range was 5 µm × 5 µm, with a scan rate of 1 Hz. The probe had a spring constant of 40 N/m and a resonance frequency of 300 kHz. Scanning electron microscopy (SEM) imaging was performed using a Sigma 500 microscope (Carl Zeiss AG, Oberkochen, Germany). For particle size analysis, a minimum of 200 particles was measured. X-ray photoelectron spectroscopy (XPS) analysis was conducted on an ESCALAB 250Xi system (Thermo Fisher Scientific, Waltham, MA, USA) with Al Kα radiation (1486.6 eV). Survey spectra were recorded at a pass energy of 160 eV, and high-resolution spectra were acquired at 20 eV pass energy. Peak fitting was carried out using the XPS Peak 4.1 software (Raymund W.M. Kwok, Chinese University of Hong Kong, Hong Kong, China), employing Gaussian–Lorentzian line shapes. Fourier transform infrared (FTIR) spectroscopy was performed on an IRTracer-100 spectrometer (Shimadzu Corporation, Kyoto, Japan) in the range of 4000–500 cm^{-1} with a resolution of 4 cm^{-1}. Samples were prepared as KBr pellets. The UV-visible absorption of the Au NPs solution was measured using a UH4150 spectrophotometer (Hitachi High-Tech Corporation, Tokyo, Japan) over the wavelength range of 400–800 nm. Nanoparticle diameters were determined with a Zetasizer Nano S90 instrument (Malvern Panalytical Ltd., Malvern, UK). Zeta potential measurements for both Au NPs and the hydrogel were obtained using a Surpass 3 system (Anton Paar GmbH, Graz, Austria) at 25 °C. All measurements were performed in triplicate, and results are expressed as mean ± standard deviation. Surface-enhanced Raman spectroscopy (SERS) spectra were collected using a portable i-Raman-785S spectrometer (Metrohm AG, Herisau, Switzerland).

Synthesis of Au NPs

180 mL of ethylene glycol solution, 3.6 mL of PDADMAC solution and 90 µL of 1 M $HAuCl_4$ aqueous solution were added to a 200 mL round-bottom flask, with adequate magnetic stirring with 500 rpm stirring speed at room temperature. Subsequently, the flask plug should be securely sealed with a raw material tape and placed in an oil bath at 185 ℃ for 60 min without stirring. After the addition of 45 µL of $HAuCl_4$ aqueous solution for chemical etching, the solution changed its color from dark red to light red. Subsequently, excess surfactants and precursors in the obtained suspension were removed through centrifugation at 12,000 rpm for 15 minutes. The centrifugation process for the surfactants was conducted three times. Aqueous solutions of Au NPs with varying concentrations (0.1 wt%, 0.5wt%) were prepared by dissolving the centrifuged products in deionized water, respectively.

Preparation of Hydrogel Film

The mixture was prepared by thoroughly combining 2 g of acrylamide, 0.05 g of MBAAm, 3 mL of acrylic acid, and 250 µL of Irgacure 2959 solution (prepared by dissolving 3.3 g of Irgacure 2959 in 10 mL of DMSO) with 10 mL of deionized water. The mol% of acrylamide and acrylic acid was 90% and 10%, respectively, with MBAAm as the crosslinker at 0.5 mol%. The cover slips were sequentially ultrasonically cleaned in alcohol and deionized water, followed by air-drying before use. A total volume of 120 µL of the mixture was applied to a coverslip, which was then gently covered with another coverslip and exposed to a UV light source (365 nm wavelength, 22 W intensity) for 20 minutes. The resulting hydrogel film, with a thickness of 200 µm as determined by a digital micrometer caliper, was subsequently immersed in deionized water and stored at 4 °C for further use.

Fabrication of Hydrogel @Au NPs Arrays

The hydrogel film was immersed in an aqueous solution of gold nanoparticles (Au NPs) at ambient temperature for 30 minutes. Subsequently, it was rinsed with deionized water to remove any unabsorbed Au NPs. The uneven edges of the hydrogel film@Au NPs were then meticulously trimmed, and the film was placed on a clean substrate for air drying. Prior to surface-enhanced Raman spectroscopy (SERS) detection, the film underwent plasma cleaning to eliminate surface residues.

Analogue Simulation

A finite-element model was created using the wave optics module of COMSOL Multiphysics 6.2 (COMSOL Group, Sweden) to better understand the electromagnetic Raman enhancement effect of hot spots based on a bistratal hydrogel@Au NPs substrate. The model simulated the global electric field distribution in the frequency domain at the microscopic scale using Maxwell's electromagnetic wave equation for the scattered electric field, E_{sca}.

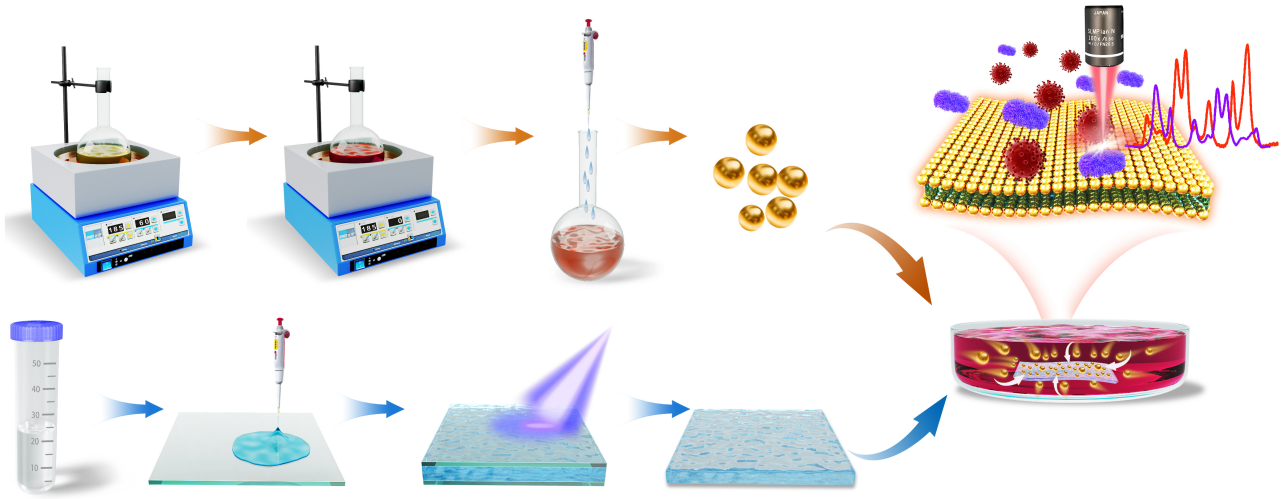

Fig. 1. Schematic illustration for the fabrication of bistratal hydrogel@Au NPs arrays by Adobe Illustrator 2023 (Version 27.0, Adobe, USA). Main procedures: (1) Synthesis of PDDA-capped Au NPs via ethylene glycol reduction; (2) Preparation of P(AAm-co-AAc) hydrogel film via UV-initiated polymerization; (3) Electrostatic adsorption of positively charged Au NPs onto negatively charged hydrogel film and air-drying; (4) SERS detection of viruses on the substrate. Au NPs, gold nanoparticles; SERS, surface-enhanced Raman scattering.

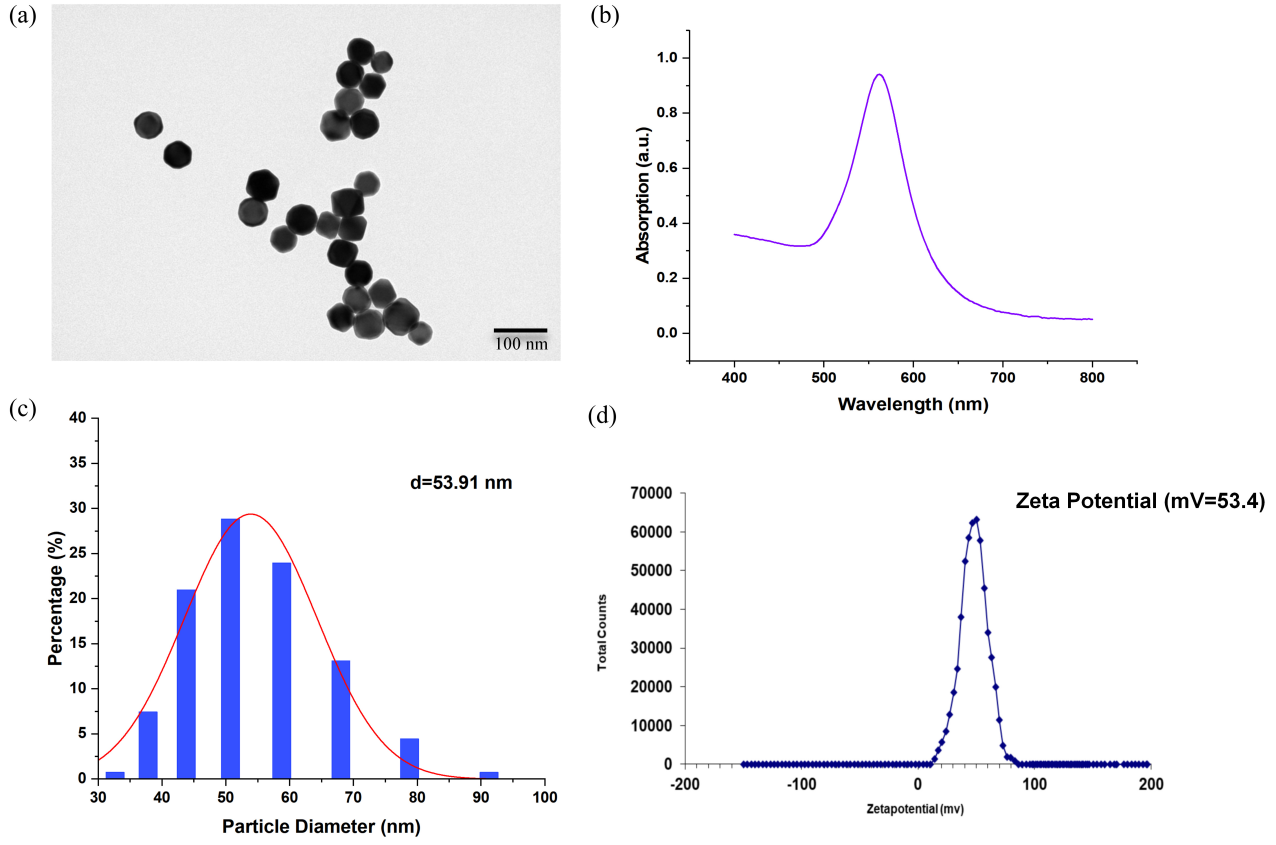

Fig. 2. Characterization of Au NPs. (a) SEM images showing the morphology of Au NPs. (b) UV-visible absorption spectra illustrating the optical properties of Au NPs. (c) Particle size distribution histogram of Au NPs (n = 200). (d) Zeta potential distribution diagram (53.4 ± 2.1 mV, with 3 independent replicate measurements). SEM, scanning electron microscopy.

$$\nabla \times \left[\frac{1}{\mu_r}\left(\nabla \times E_{sca}\right)\right] - K_0^2\left[\left(\varepsilon_\gamma - \frac{j\sigma}{\omega\varepsilon_0}\right)\right] E_{sca} = 0$$

w E_{sca} – scattered electric field
K_0 – wavenumber in free space
μ_r – relative permeability of medium
ε_γ – permittivity of medium

Au NPs were simulated as scatterers using the electromagnetic wave frequency domain interface, and perfectly matched layers (PML) were introduced in the geometry of the substrate model. The full-field solution obtained in the first interface was used as the background field, and only the scattering field needed to be absorbed in the PML. The simulation was performed under two port conditions. One of the z-direction upper surfaces was defined as the incident plane wave, while absorbing the reflected wave reflected by the specular surface. The other port was optimised to absorb plane waves transmitted by the substrate. Moreover, the side boundary was set as the Floquet condition, indicating that the solution on one side of the geometry is equal to the solution on the other side multiplied by the complex-valued phase factor. Under the aforementioned parameters, the model was effectively constructed as a portion of a geometry, eternally extending along the parallel plane of the substrate.

The input parameters of the periodic port were determined by the direction of propagation and the polarization of the incident electric field. This information was also utilized to satisfy the Floquet condition internally. Incident wave:

$$\mathbf{k}_a = (k_x, k_y, k_z) = k_a\left(\cos\phi_a \sin\theta_a, \sin\phi_a \cos\theta_a, -\cos\theta_a\right)$$

$\mathbf{k}_a$ – wavenumber in the first medium
ϕ_a – incidence azimuth angle
θ_a – polar angle

The equation representing the tangential polarized electric field vector within the plane of incidence is:

$$\mathbf{E}_0 = E_0\left(-\sin\phi_a, \cos\phi_a, 0\right)\exp\left(-\mathrm{i}\left(k_x x + k_y y\right)\right)$$

The "port" state facilitated the determination of the overall input power, which was subsequently utilized to calculate the magnitude of the electric field, denoted as:

$$P = I_0 A\cos\theta$$

I_0 – the intensity of the incident field
A – the boundary area of the set port

SERS Measurement

The active Raman molecules, crystal violet and malachite green, were prepared at varying concentrations to assess the detection performance of the substrate. Solutions containing SARS-CoV-2 spike protein pseudovirus and Mpox B6R pseudovirus were separately diluted to different concentrations for experimental evaluation. The used pseudoviruses are replication-incompetent and classified as Biosafety Level 2 (BSL-2) agents, handled in compliance with BSL-2 laboratory regulations. SERS spectra were collected using a portable Raman spectrometer i-Raman-785S (Metrohm, Switzerland) with a 785 nm laser, ×50 objective lens, 60 mW laser power, and 15 s acquisition time. For probe molecules (crystal violet and malachite green), solutions were prepared at concentrations of 10^{-5} M, 10^{-7} M, 10^{-8} M, 10^{-9} M, 10^{-10} M, 10^{-11}M, and 10^{-12} M. For viral pseudoviruses, solutions were diluted to concentrations of 10^6 TU/mL, 10^5 TU/mL, 10^4 TU/mL, 10^3 TU/mL, 10^2 TU/mL, 10 TU/mL, and 1 TU/mL. A 1 µL sample was spotted onto the substrate surface and allowed to air-dry before detection. Each sample was measured at 3 different spots to ensure reproducibility.

Statistical Analysis

Linear regression analysis was performed using Origin 2024 software (Origin lab, USA) to establish calibration curves correlating Raman intensity with concentration, with R^2 values calculated to assess linearity. Principal Component Analysis (PCA) was conducted using the built-in tool in Origin 2024, with preprocessing steps including vector normalization and mean-centering. Distinct characteristic peaks were used for clustering and differentiating samples.

Results

Fabrication of Bistratal Hydrogel@Au NPs Arrays

An electrostatic adsorption self-assembly strategy was employed for the fabrication of bistratal hydrogel@Au NPs arrays [27], as illustrated in Fig. 1. Ethylene glycol was used as a reducing agent to reduce $HAuCl_4$ to nanoparticles. The corner or shape edge of the Au NPs was removed from the gold colloid after it had been obtained by adding a moderate amount of $HAuCl_4$ solution for the chemical etching process. Fig. 2a presents negatively stained images of Au NPs, which are uniform spherical nanoparticles with an average diameter of 53.91 nm, smooth surfaces and minimal aggregation. Fig. 2b displays the UV-visible absorption spectrum of the Au NPs, with a characteristic absorption peak at 562 nm. Fig. 2c shows additional SEM images confirming the uniform Au nanospheres, consistent with the average diameter of 53.91 nm. PDDA, not only an electronic conducting polymer but also a cationic polymer, was utilized to synthesis PDDA-capped Au NPs [28,29]. The positively charged Au NPs with 53.4 ± 2.1 mV (Fig. 2d) were applied to be absorbed onto the negatively charged hydrogel film.

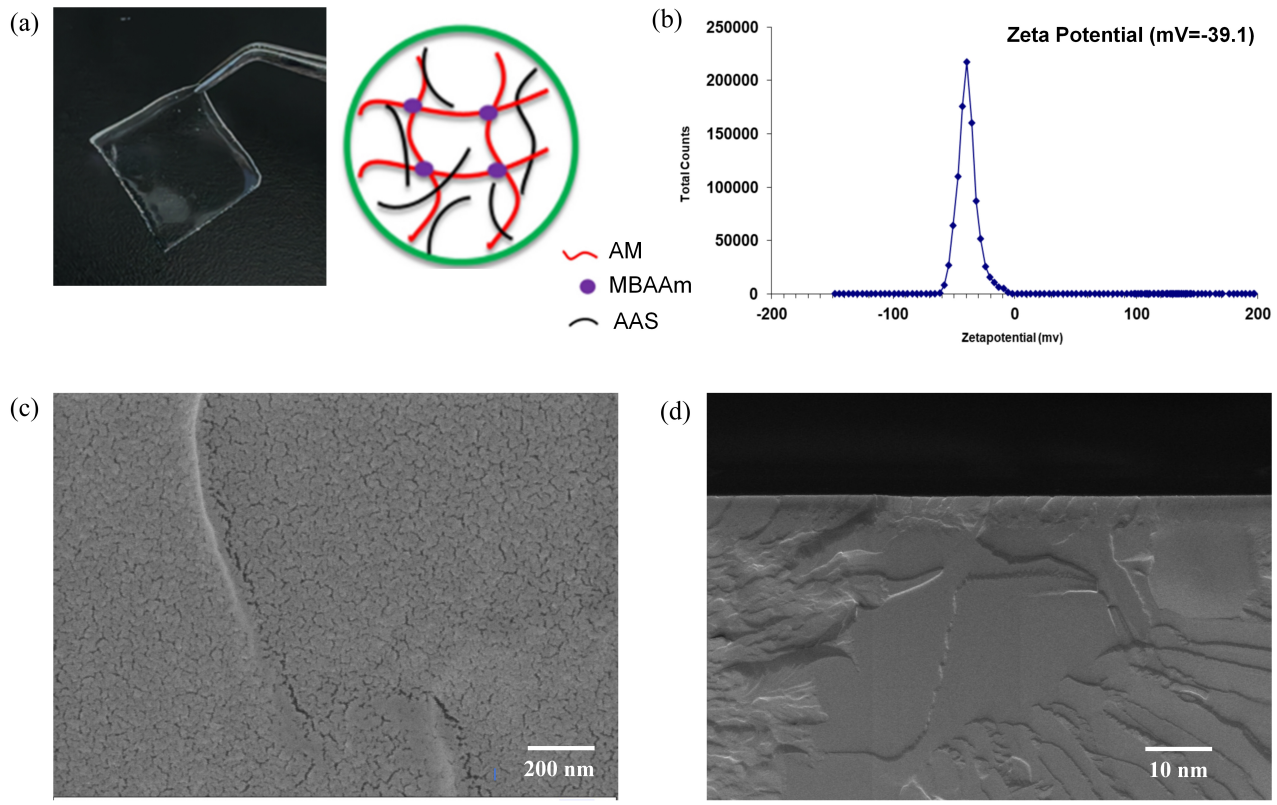

Fig. 3. Characterization of P(AAm-co-AAc) hydrogel film. (a) Digital photograph and schematic illustration of the structure. (b) Zeta potential distribution diagram (–39.1 ± 2.1 mV, with 3 independent replicate measurements). (c) Planar SEM images at 200 nm. (d) Cross-sectional SEM images at 10 nm.

Furthermore, a Poly(acrylamide-co-acrylic acid) [P(AAm-co-AAc)] hydrogel (Fig. 3a) was synthesized via free-radical crosslinking copolymerization using a constant amount of AAm monomer and varying quantities of AAc as the ionic comonomer [30]. As depicted in Fig. 3b, a zeta potential of –39.1 ± 1.5 mV verified the negative surface charge of the P(AAm-co-AAc) hydrogel film, attributable to the hydrolysis of carboxyl groups in AAc into carboxylate anions (-COO-). The planar SEM image (Fig. 3c) exhibits a smooth surface morphology of the pristine hydrogel at a 200 nm scale. A cross-sectional SEM image (Fig. 3d) further reveals a uniform internal porous structure.

Subsequently, the concentrations of AAc and Au NPs were systematically optimized. At initial concentrations of 10 wt% AAc and 0.5 wt% Au NPs, the hydrogel surface displayed sparse and random adsorption of Au NPs. Increasing the Au NP concentration to 0.8 wt% led to the formation of a uniform, densely packed monolayer upon drying, with interparticle spacings of less than 10 nm. However, increasing the acrylic acid concentration hindered monolayer formation, promoting the adsorption of Au NPs in multilayered configurations instead. The optimized formulation—0.8 wt% Au NPs and 10 wt% acrylic acid—was used to fabricate a substrate featuring active nanogaps. As shown in Fig. 4a, the hydrogel membrane was initially immersed in a solution of Au NPs. Fig. 4b displays the resulting wet-phase film after 30 mins of self-assembly, indicating progressive nanoparticle deposition. Upon drying, a golden, highly reflective substrate featuring active nanogaps was successfully produced, as illustrated in Fig. 4c. The dynamic evolution of the assembly process is captured in Fig. 4d,e after 1 min and 15 mins, respectively: Fig. 4d reveals sparse adsorption of Au NPs on the film surface, while Fig. 4e shows a pronounced increase in nanoparticle density, a decrease in interparticle distance, and the initial formation of small clusters. Further optimization during drying yielded a uniform, closely packed nanoparticle array with interparticle gaps below 10 nm (Fig. 4f).

Structural Characterization

Atomic Force Microscopy (AFM) was utilized to characterize the surface morphology of the hydrogel film@Au NPs. The 2D and 3D AFM images presented in Fig. 5 reveal a substrate with an average height of approximately 50 nm. As shown in Fig. 5a, statistical parameters derived from the height distribution function include a root mean square roughness (Sq) of 3.169 nm and an arith-

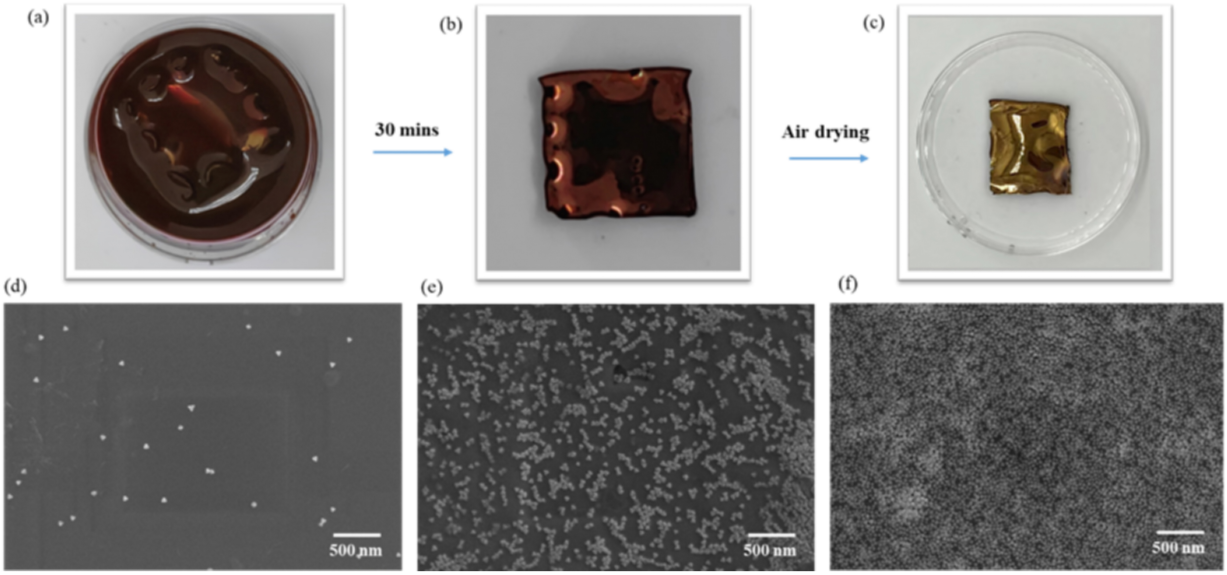

Fig. 4. SEM images of hydrogel@Au NPs. (a) Hydrogel film immersed in Au NPs solution. (b) Hydrogel film@Au NPs after self-assembly for 30 mins (wet phase). (c) Hydrogel film@Au NPs (dry phase). (d) SEM image of hydrogel@Au NPs after self-assembly for 1 min. (e) SEM image of hydrogel film@Au NPs after self-assembly for 15 min. (f) SEM image of hydrogel film@Au NPs after self-assembly for 30 mins.

metic mean roughness (Sa) of 2.470 nm. Extreme value parameters indicate a maximum peak height (Sp) of 8.38 nm and a maximum pit depth (Sv) of 15.07 nm. Additionally, the inter-particle spacingbetween nanoparticles, as illustrated in Fig. 5b, is approximately 6 nm. These findings indicate that the hydrogel film@Au NPs exhibit a highly uniform and controlled surface structure, which is essential for their prospective applications in sensing and catalytic processes. The narrow interstitial spaces between nanoparticles, coupled with the negatively charged surface, create an optimal platform for further functionalization and interaction with target molecules. Moreover, the observed roughness parameters suggest a relatively smooth yet textured surface, facilitating efficient contact and adhesion of analytes. Such structural characteristics are anticipated to enhance the material's performance in subsequent experimental stages, particularly when integrated into devices that require precise nanoscale arrangements.

We also identified the characteristic peaks of infrared spectroscopy originating from the substrate (Fig. 6a). The spectrum of PDDA protected Au NPs was similar to that of original PDDA, providing a broad and large peak at 3387 cm^{-1} of N-H stretching vibration or hydroxyl group, double peaks at 2947 and 2882 cm^{-1} corresponding to the stretching vibration of C-H groups, peaks at 1640 and 1461 cm^{-1} of the stretching vibration of C-O, and bands at 1535 cm^{-1} of C-N stretching and bending vibration [31,32]. In the FT-IR spectra of hydrogel, peaks detected at 3341 and 3196 cm^{-1} were attributed to asymmetric and symmetric stretching vibrations of N-H, while the peaks at 1650 and 1603 cm^{-1} represent the amide-I and amide-II bands of PAM, respectively [33,34]. The bands at 1243, 1173 cm^{-1} verified the presence of the C-H groups of polymers P(AAm-co-PAA) in the corresponding bonds, and the appearance of small peaks in the range of 2931 and 1447 cm^{-1} was caused by the angular vibration of methylene [35]. After the formation of the hydrogel@Au film, it was noted that most absorption peaks were similar to those of hydrogel, and new peaks at 1084 and 1038 cm^{-1} responded to the C-O stretching vibration of PDDA-protected Au NPs. These results demonstrated the effective formation of a composite film, indicating that the hydrogel@Au NPs substrate was fabricated mainly by physical adsorption.

As shown in Fig. 6b, XPS was carried out to further determine the contribution of all functional groups in the adsorption demonstration. The hydrogel film before and after Au NPs absorbed exhibited the strong signals related to C, O, N and Au. The C1s spectra of the hydrogel@Au NPs (Fig. 6c) were fitted by three peaks, the main peak corresponding to C-C and C-H at 284.8 eV, C=O at 286.2 eV, and C-N at 288.2 eV, when compared with the XPS of the hydrogel without a significant change [36]. The N1s spectrum (Fig. 6d) and O1s spectrum (Fig. 6e) clearly evidenced the presence of amide groups presented on the hydrogel surface both before and after electrostatic adsorption [37]. The Au spectrum (Fig. 6f) exhibited two contributions, Au $4f_{7/2}$ and Au $4f_{5/2}$ (resulting from the spin-orbit splitting), located at 83.9 and 87.6 eV, respectively [38]. After self-assembling, conspicuous peaks of Au 4f were observed in the wide scan XPS spectra, evidencing the successful adsorption of Au NPs onto the hydrogel film.

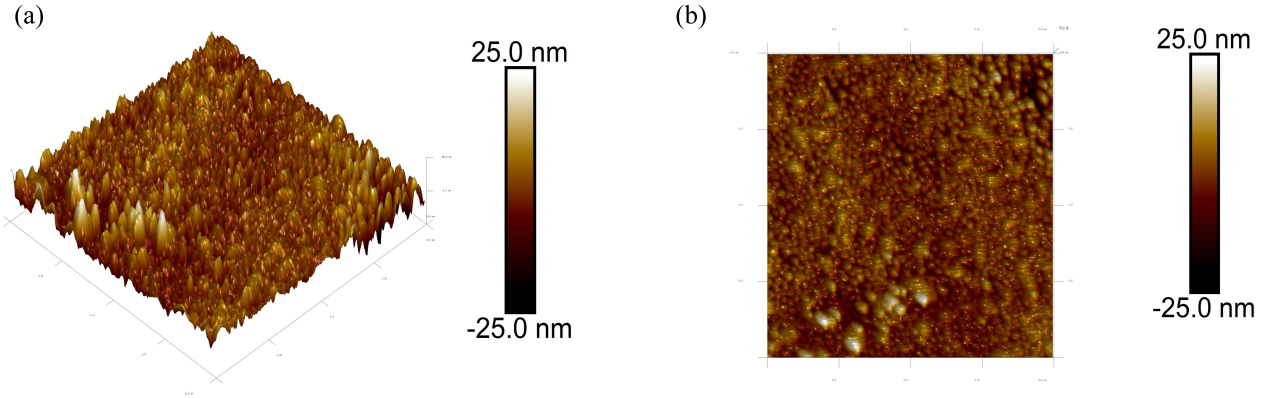

Fig. 5. AFM images of hydrogel film functionalized with gold nanoparticles (Au NPs). (a) Three-dimensional topographical structure. (b) Planar topographical structure. AFM, atomic force microscopy.

Analogue Simulation Calculation

A simulation area of 500 nm × 500 nm was constructed using spherical Au NP arrays with an interparticle gap of 6 nm. The refractive indices for Au NPs and the hydrogel were set as 1.625 + 1.750i and 1.4 + 0i, respectively. A comparison of the electric field enhancement produced by single-layer, and bistratal Au NPs arrays was conducted using the aforementioned parameters. Fig. 7 presents finite-element simulations of the electric-field enhancement for the hydrogel@Au NPs substrate, providing a systematic analysis of its structural evolution and electromagnetic properties. Fig. 7a shows a cross-sectional view of the pristine hydrogel layer, revealing the smooth polymer network of the bare P(AAm-co-AAc) substrate as a reference. Following electrostatic adsorption, a dense bilayer array of Au NPs is uniformly formed on the hydrogel surface, as illustrated in Fig. 7b. Simulations of the electromagnetic field intensity in Fig. 7c reveal a pronounced near-field enhancement at interparticle hotspots, reaching approximately 20 times that of single-layer structures and an overall enhancement factor of ~10^6. Fig. 7d–f depicts the gap-dependent electromagnetic coupling in the bilayer Au NP arrays: the optimized 6 nm gap (Fig. 7d) yields the highest near-field intensity with strongly localized hotspots; the 7 nm gap (Fig. 7e) exhibits moderate coupling due to the increased interparticle distance; and the 8 nm gap (Fig. 7f) leads to further attenuation of the field enhancement. This effect arises from the superposition of electric fields among adjacent Au NPs, leading to a significant amplification of the "hot spots" and a resultant overall field enhancement of approximately 10^6.

Verification of Hot Spots SERS Activity

The SERS performance of the prepared substrate was evaluated using crystal violet (CV) and malachite green (MG) as probe molecules. Despite the additional tertiary amine group in CV, both CV and MG exhibit similar chemical structures, as shown in Fig. 8a. Upon adding 1 µL of 10^{-5} M CV aqueous solution on the hydrogel@Au NPs substrate, the spectrum exhibited strong enhancement of the vibrational bands at 1585, 1536, 1389, 1299, 1174, 915, 798, 724 and 526 cm^{-1}. Similarly, 1 µL of 10^{-5} M MG solution also showed enhanced peaks at at 1585, 1536, 1391, 1174, 915, 798, 724 and 526 cm^{-1}. Owing to the presence of an additional tertiary amine group in CV, the band at 1299 cm^{-1} displayed a more prominent characteristic peak attributed to ring C-C stretching vibrations [39]. Under optimal conditions, the hydrogel@Au NPs arrays demonstrated excellent SERS activity for both CV and MG, achieving detection limits of 2.45 × 10^{-11} M for CV and 2.71 × 10^{-11} M for MG at the 1174 cm^{-1} peak. Calibration curves constructed utilizing the SERS peak intensities at 1174 cm^{-1} for CV resulted in an R-square (R^2) value of 0.997 (Fig. 8b), whereas MG demonstrated an R^2 value of 0.996 at the identical peak position (Fig. 8c).

Rapid SERS Detection of SARS-CoV-2 and Mpox

Several efforts have been made to leverage the SERS platform for the rapid identification of various viral pathogens. Studies indicate that enveloped viruses can be detected label-free due to their characteristic lipid envelopes and protein compositions—including phospholipid bilayers, cholesterol, and envelope glycoproteins—which produce distinct Raman fingerprints in the 1000–1600 cm^{-1} region. To evaluate the adaptability of this method for detecting novel viruses, we tested SARS-CoV-2 Spike pseudoviruses and Mpox B6R pseudoviruses. For the SARS-CoV-2 Spike pseudovirus (Fig. 9a), characteristic Raman bands were observed at 1324, 1266, 1140, 1058, and 831 cm^{-1}, attributed to Tryptophan (Trp) and Amide III (α-Helix). Fig. 9b displays analogous SERS spectra for Mpox B6R pseudovirus over the same concentration range, exhibiting key Raman bands at 1077 cm^{-1} and other fingerprint regions.

The intensity of the Raman peak at 1324 cm^{-1} exhibited a strong linear relationship with virus concentra-

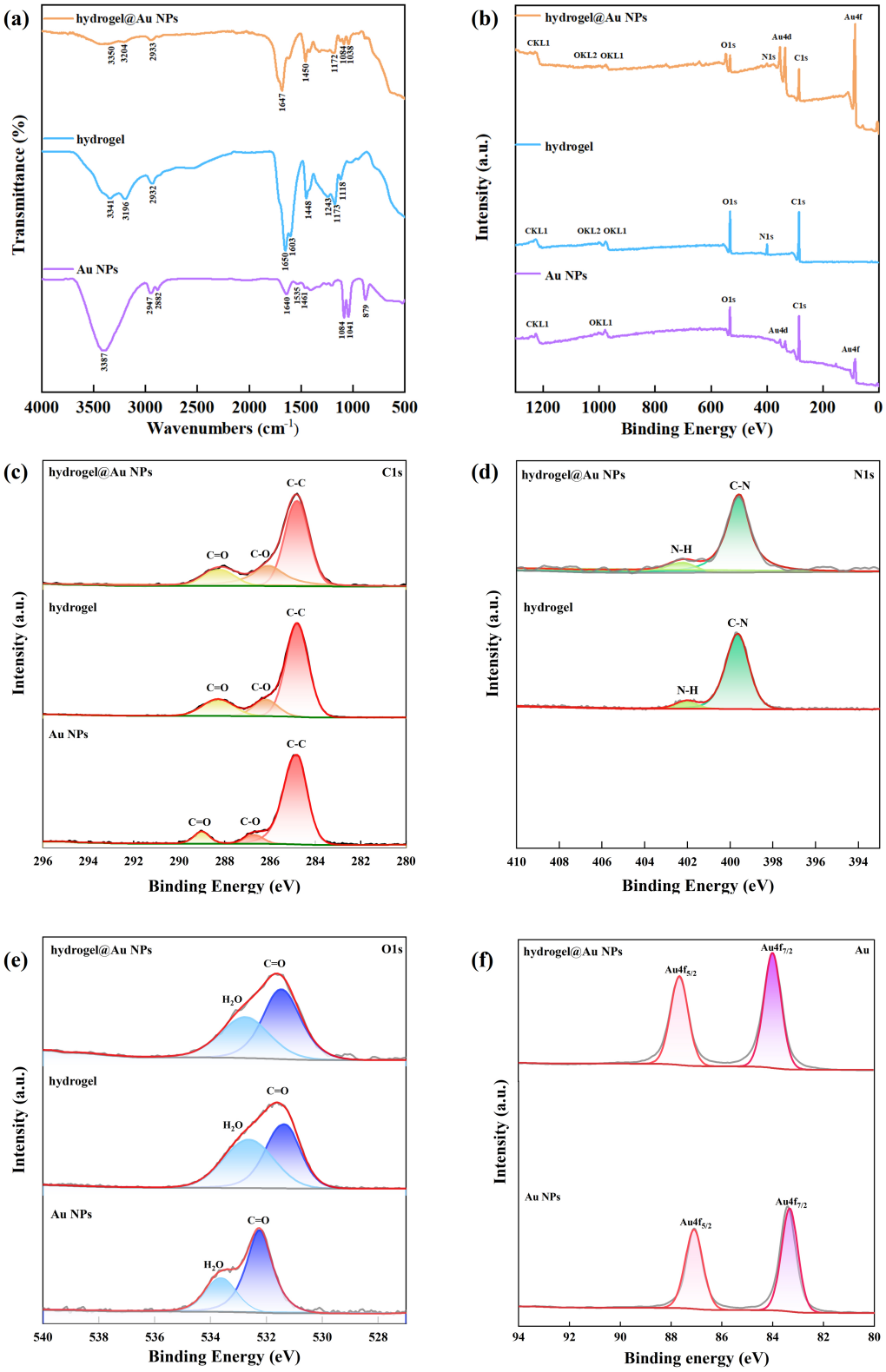

Fig. 6. FT-IR spectroscopy and XPS survey of hydrogel film@Au NPs, hydrogel and Au NPs. (a) FT-IR spectra of hydrogel film@Au NPs, hydrogel, and Au NPs. (b) XPS full spectra of hydrogel film@Au NPs, hydrogel, and Au NPs. (c) High-resolution XPS spectrum of C1s. (d) High-resolution XPS spectrum of N1s. (e) High-resolution XPS spectrum of O1s. (f) High-resolution XPS spectrum of Au4f. XPS, X-ray photoelectron spectroscopy.

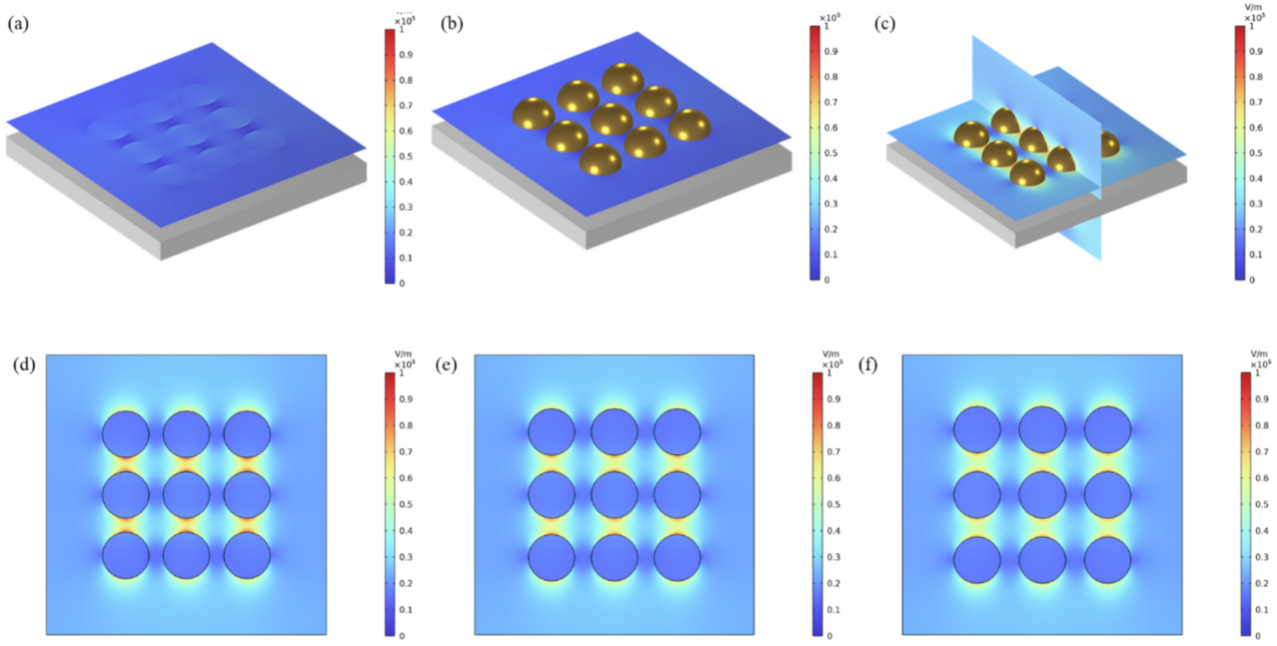

Fig. 7. Finite element modelling of electric-field enhancement based on hydrogel@Au NPs substrate. (a) Cutting surface construction of the hydrogel layer. (b) Cutting surface of the hydrogel layer adsorbed by Au NPs. (c) Electromagnetic field intensity simulation of double-layer Au NPs adsorption on hydrogel. (d) XY cross-seciton of double layer Au NPs array with a 6 nm gap. (e) XY cross-seciton of double-layer Au NPs array with a 7 nm gap. (f) XY cross-seciton of double-layer Au NPs array with a 8 nm gap.

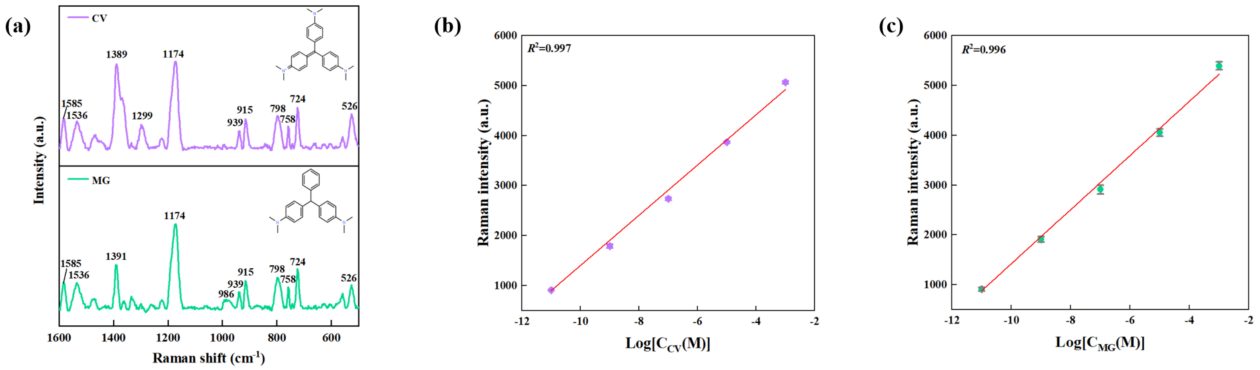

Fig. 8. SERS spectra and linear regression curve of CV and MG aqueous solution. (a) SERS spectra of 1 µL of 10^{-5} M CV and 1 µL of 10^{-5} M MG aqueous solution separately on the hydrogel@Au NPs substrate. (b) The corresponding relationship between the Raman intensity at 1174 cm^{-1} and the varying concentrations of CV. (c) The corresponding relationship between the Raman intensity at 1174 cm^{-1} and the varying concentrations of MG. CV, crystal violet; MG, malachite green.

tion, with an R2 value of 0.997. Fig. 9c provides spectral reproducibility validation through 20 random SERS measurements of SARS-CoV-2 at 10^3 TU/mL, demonstrating minimal spectral variance. Fig. 9d shows corresponding 20-replicate spectra for Mpox at 10^3 TU/mL, confirming consistent signal enhancement across independent samples. Fig. 9e illustrates the calibration curve for SARS-CoV-2 based on the linear relationship between Raman intensity at 1324 cm^{-1} and logarithmic virus concentration, achieving an R^2 value of 0.997. Similarly, for the Mpox B6R pseudovirus, the intensity of the Raman peak at 1077 cm^{-1} was positively correlated with the logarithm of the virus concentration within the range of 1 TU/mL to 10^6 TU/mL, with an R2 value of 0.997 (as shown in Fig. 9f). Fig. 10 shows the PCA results indicate that our method can accurately capture the SARS-CoV-2 and Mpox fingerprints and identify the viruses in the biological background within 1 min. Fig. 10a shows distinct clustering of 20 SARS-CoV-2 positive samples, while Fig. 10b reveals clear separation of 10 Mpox clinical samples from negative controls, with minimal overlap between groups. This clear demarcation validates that the SERS fingerprints captured by our hydrogel@Au NPs

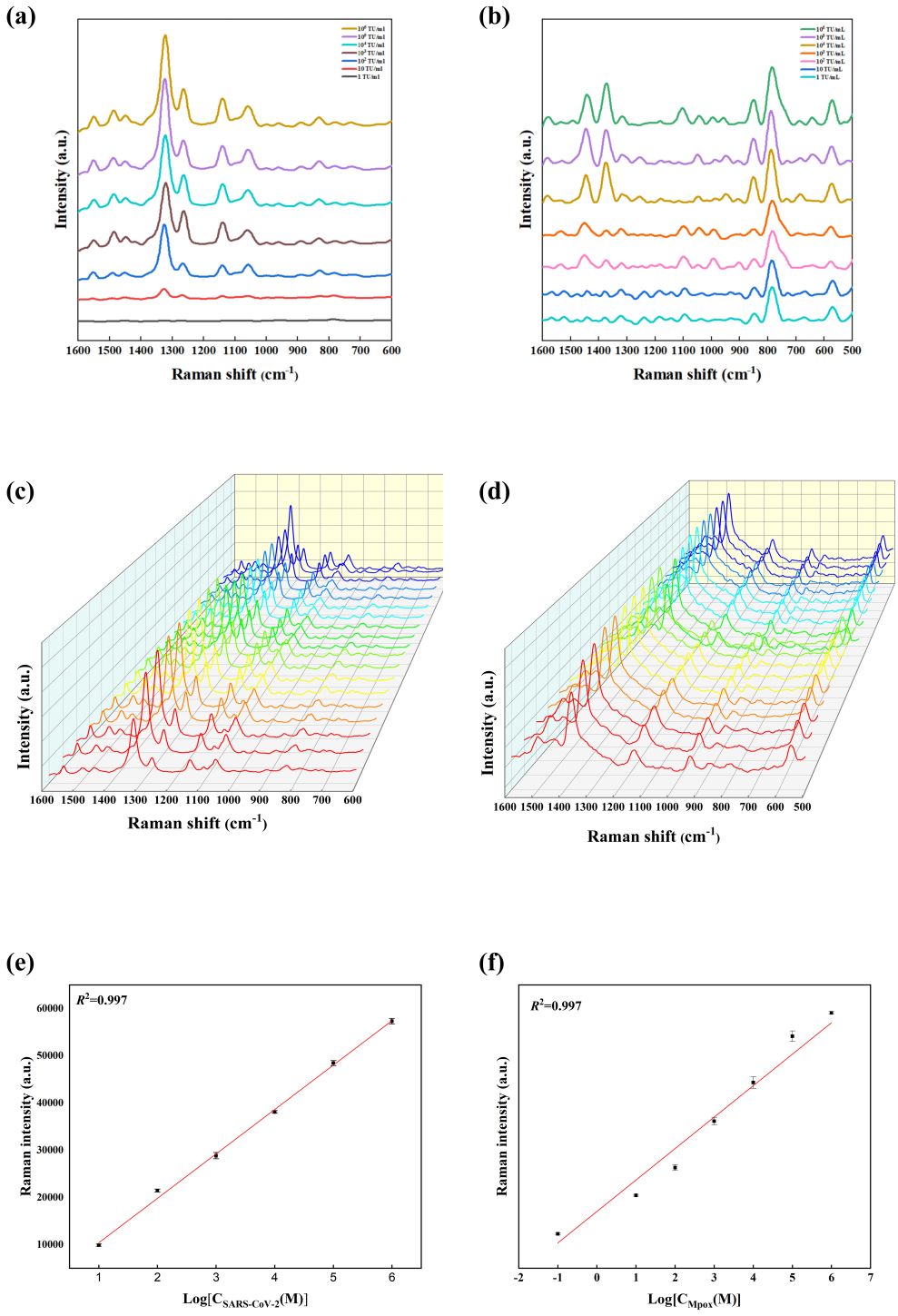

Fig. 9. SERS detection of SARS-CoV-2 Spike pseudovirus and Mpox B6R pseudovirus under the excitation laser of 785 nm. (a) SERS detection of SARS-CoV-2 Spike pseudovirus with different concentrations (from 1 TU/mL to 10^6 TU/mL). (b) SERS detection of Mpox B6R pseudovirus with different concentrations (from 1 TU/mL to 10^6 TU/mL). (c) SERS spectra provided by random 20 groups of (10^3 TU/mL) samples of SARS-CoV-2 Spike pseudovirus. (d) SERS spectra provided by random 20 groups of (10^3 TU/mL) samples of Mpox B6R pseudovirus. (e) The calibration curve of SARS-CoV-2 Spike pseudovirus with Raman intensity at 1324 cm^{-1}. (f) The calibration curve of Mpox B6R pseudovirus with Raman intensity at 1077 cm^{-1}. SARS-CoV-2, severe acute respiratory syndrome coronavirus 2.

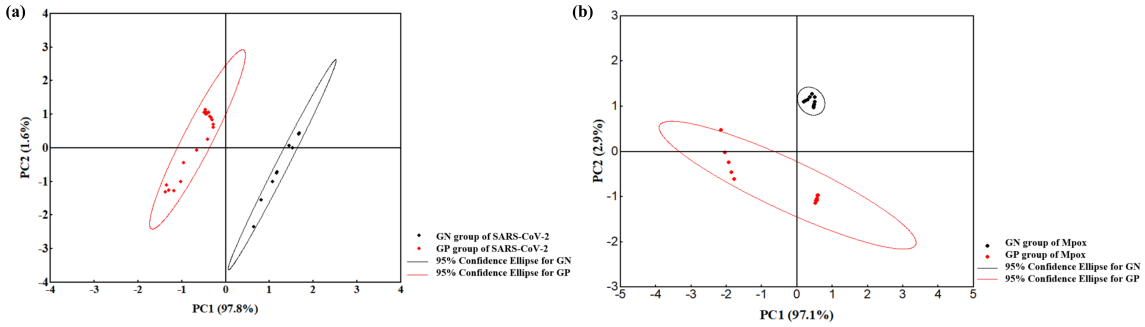

Fig. 10. Results of PCA for SERS detection of clinical samples. (a) PCA calculation of 20 clinical positive samples and 10 negative samples with SARS-CoV-2. (b) PCA calculation of 10 clinical positive samples and 10 negative samples with Mpox. PCA, Principal Component Analysis.

substrate are specific and reproducible across different viral pathogens and biological matrices. The tight clustering within each viral group indicates excellent reproducibility across multiple substrate batches and sample preparations, addressing a critical challenge in SERS-based diagnostics.

Discussion

This study presents the development of a bistratal hydrogel@Au nanoparticles array-based surface-enhanced Raman spectroscopy (SERS) technique for the rapid detection of novel viruses. The core innovation of this technology lies in utilizing the drying and shrinking properties of hydrogel film to reduce the interparticle distance from random spacing to approximately 6 nm, thereby forming uniformly dense "hot spot" structures that significantly enhance the local electromagnetic field. This self-assembly method not only features a simple process and low cost but also enables highly reproducible substrate preparation, providing a new technical platform for virus detection [25,39].

Compared with existing virus detection technologies, the SERS method proposed in this study demonstrates notable advantages. Traditional nucleic acid amplification tests, although highly sensitive, require professional laboratory equipment and complex operational procedures. In contrast, antigen- or antibody-based assays, though rapid, often suffer from insufficient sensitivity and a higher risk of false-positive issues. The SERS technology developed in this study requires no labeling steps and can directly detect virus molecules, achieving a limit of detection (LOD) of 1 TU/mL for both SARS-CoV-2 Spike pseudovirus and Mpox B6R pseudovirus, showing excellent linear responses ($R^2 > 0.997$). Furthermore, this method enables complete detection within 1 minute, greatly improving rapid response capabilities in emergencies.

From a technical perspective, this study achieves the electrostatic self-assembly of positively charged Au nanoparticles (zeta potential: 53.4 ± 2.1 mV) onto the surface of negatively charged hydrogel film (zeta potential: -39.1 ± 1.5 mV). During the drying process of the hydrogel, its volume contraction reduces interparticle spacing, forming a dense "hot spot" structure. Finite element simulation results indicate that the bistratal hydrogel@Au nanoparticles array structure enhances the electromagnetic field intensity by approximately 20-fold compared to a single-layer structure, ultimately achieving an overall SERS enhancement factor of about 10^6. This enhancement mechanism mainly originates from the LSPR effect and near-field coupling between particles.

The methodological innovations of this study are reflected in multiple aspects. First, by optimizing the concentration of acrylic acid (AAc, 10 wt%) and Au nanoparticles (0.8 wt%), uniform adsorption and close arrangement of nanoparticles are achieved. Second, employing the hydrogel as a spacer avoids the high cost and complexity of traditional lithography technologies [40]. Third, this method is highly scalable and adaptable for detecting different types of viruses [41]. Additionally, the technology shows excellent performance, achieving detection limits as low as 10^{-11} M for probe molecules such as CV and MG, fully verifying its high sensitivity characteristics. The prefabricated hydrogel@Au NPs arrays can be stored in deionized water at 4 °C for up to 4 weeks without significant loss of SERS activity. For long-term storage, the arrays can be lyophilized and rehydrated before use, making them suitable for field deployment and point-of-care applications.

Although this study has achieved significant progress, there are still some limitations that need to be addressed. First, while the study confirms the ability of this technology to detect SARS-CoV-2 and Mpox, it has not yet been validated across large-scale clinical samples encompassing virus strains.

Second, its anti-interference performance in complex biological matrices needs further evaluation. Furthermore, although the limit of LOD reaches 1 TU/mL, even higher sensitivity may be required in practical settings to detect low viral loads during the early stages of infection.

Future investigations can be performed from the following aspects: first, applying this technology to detect a

broader range of novel viruses to evaluate its generalizability. Second, developing portable SERS devices combined with microfluidic technology for automated sample processing, enabling truly rapid on-site detection. Third, further optimizing the structure of hydrogel@Au nanoparticle arrays to explore the effects of different nanoparticle shapes and sizes on SERS performance. Finally, developing more advanced SERS data analyses by combining machine learning and deep learning algorithms to improve detection accuracy and reliability.

The technical innovation of this study lies in combining the self-shrinking effect of the hydrogel film with the plasmonic resonance properties of Au nanoparticles, creating a simple and efficient method for fabricating an SERS substrate. This design is not only suitable for virus detection but can also be extended to other biomarker detection fields, with broad potential for diverse applications. With continuous optimization and improvement, this SERS-based rapid detection technology is expected to become an important tool for responding to future outbreaks, providing strong support for public health security.

Conclusion

In this study, we successfully fabricated bistratal hydrogel@Au NPs arrays via a self-assembly strategy based on electrostatic adsorption. The hydrogel acts as an effective spacer, reducing the interparticle distance between gold nanoparticles and facilitating the formation of a uniform, densely packed, high-quality substrate. This approach significantly enhances the sensitivity of Raman detection, providing a promising platform for rapid identification of emerging viruses.

The future applications of this method can be highlighted in two major aspects. Firstly, multiplex pathogen detection can be achieved by the inherent multispectral resolution capabilities of SERS. Secondly, integration with portable devices for point-of-care testing holds great promise, potentially enabling rapid on-site detection in community clinics, airports, and schools, thereby supporting “early detection and isolation” strategies during infectious disease outbreaks.

Availability of Data and Materials

All raw data and code are available upon request from the corresponding author.

Author Contributions

Conceptualization, YL and ZG; methodology, YL, YC, and ZG; software, YL; validation, YL and YC; formal analysis, YL, YC, and ZG; investigation, YL, YC and ZD; resources, YL, YC, and ZD; data curation, YL and ZD; writing—original draft preparation, YL; writing—review and editing, YL, YC, ZD, and ZG; visualization, YL and YC; supervision, ZG; project administration, ZG; funding acquisition, ZG. All authors have read and agreed to the published version of the manuscript. All authors agreed to be accountable for all aspects of the work in ensuring that questions related to the accuracy or integrity of any part of the work are appropriately investigated and resolved.

Ethics Approval and Consent to Participate

Ethical approval was granted by the Medical Ethics Committee of Tianjin Medical University General Hospital (IRB approval number: 2025-KY-533).

Acknowledgment

Not applicable.

Funding

This work was funded by the National Key Research and Development Program of China (2022YFF1103100).

Conflict of Interest

The authors declare no conflict of interest.

References

[1] Yao H, Song Y, Chen Y, Wu N, Xu J, Sun C, *et al*. Molecular Architecture of the SARS-CoV-2 Virus. Cell. 2020; 183: 730–738.e13. https://doi.org/10.1016/j.cell.2020.09.018.

[2] Hong Y, Huang B, Zhang J, Peng C, Kong W, Tan W, *et al*. Molecular architecture of monkeypox mature virus. Cell Discovery. 2024; 10: 108. https://doi.org/10.1038/s41421-024-00741-5.

[3] Algammal AM, Shafiq M. Monkeypox Resurgence: A Global Health Challenge Navigating Zoonotic Spillover, Genomic Evolution, and Strategic Response. Discovery Medicine. 2024; 36: 2309–2312. https://doi.org/10.24976/Discov.Med.202436190.212.

[4] Zhou Y, Zhang L, Xie YH, Wu J. Advancements in detection of SARS-CoV-2 infection for confronting COVID-19 pandemics. Laboratory Investigation; a Journal of Technical Methods and Pathology. 2022; 102: 4–13. https://doi.org/10.1038/s41374-021-00663-w.

[5] Lim CK, Roberts J, Moso M, Liew KC, Taouk ML, Williams E, *et al*. Mpox diagnostics: Review of current and emerging technologies. Journal of Medical Virology. 2023; 95: e28429. https://doi.org/10.1002/jmv.28429.

[6] Zhao F, Wang P, Wang H, Liu S, Sohail M, Zhang X, *et al*. CRISPR/Cas12a-mediated ultrasensitive and on-site monkeypox viral testing. Analytical Methods: Advancing Methods and Applications. 2023; 15: 2105–2113. https://doi.org/10.1039/d2ay01998a.

[7] Xiong E, Jiang L, Tian T, Hu M, Yue H, Huang M, *et al*. Simultaneous Dual-Gene Diagnosis of SARS-CoV-2 Based on CRISPR/Cas9-Mediated Lateral Flow Assay. Angewandte Chemie (International Ed. in English). 2021; 60: 5307–5315. https://doi.org/10.1002/anie.202014506.

[8] Azmi I, Faizan MI, Kumar R, Raj Yadav S, Chaudhary N, Kumar Singh D, *et al*. A Saliva-Based RNA Extraction-Free Workflow Integrated With Cas13a for SARS-CoV-2 Detection. Frontiers in

Cellular and Infection Microbiology. 2021; 11: 632646. https://doi.org/10.3389/fcimb.2021.632646.

[9] Robosa RS, Sandaradura I, Dwyer DE, O'Sullivan MVN. Clinical evaluation of SARS-CoV-2 point-of-care antibody tests. Pathology. 2020; 52: 783–789. https://doi.org/10.1016/j.pathol.2020.09.002.

[10] Krüttgen A, Cornelissen CG, Dreher M, Hornef MW, Imöhl M, Kleines M. Comparison of the SARS-CoV-2 Rapid antigen test to the real star Sars-CoV-2 RT PCR kit. Journal of Virological Methods. 2021; 288: 114024. https://doi.org/10.1016/j.jviromet.2020.114024.

[11] Drain P, Sulaiman R, Hoppers M, Lindner NM, Lawson V, Ellis JE. Performance of the LumiraDx Microfluidic Immunofluorescence Point-of-Care SARS-CoV-2 Antigen Test in Asymptomatic Adults and Children. American Journal of Clinical Pathology. 2022; 157: 602–607. https://doi.org/10.1093/ajcp/aqab173.

[12] Itoh T, Procházka M, Dong ZC, Ji W, Yamamoto YS, Zhang Y, *et al*. Toward a New Era of SERS and TERS at the Nanometer Scale: From Fundamentals to Innovative Applications. Chemical Reviews. 2023; 123: 1552–1634. https://doi.org/10.1021/acs.chemrev.2c00316.

[13] Pilot R, Signorini R, Durante C, Orian L, Bhamidipati M, Fabris L. A Review on Surface-Enhanced Raman Scattering. Biosensors. 2019; 9: 57. https://doi.org/10.3390/bios9020057.

[14] Das GM, Managò S, Mangini M, De Luca AC. Biosensing Using SERS Active Gold Nanostructures. Nanomaterials (Basel, Switzerland). 2021; 11: 2679. https://doi.org/10.3390/nano11102679.

[15] Wang HL, You EM, Panneerselvam R, Ding SY, Tian ZQ. Advances of surface-enhanced Raman and IR spectroscopies: from nano/microstructures to macro-optical design. Light, Science & Applications. 2021; 10: 161. https://doi.org/10.1038/s41377-021-00599-2.

[16] Wy Y, Jung H, Hong JW, Han SW. Exploiting Plasmonic Hot Spots in Au-Based Nanostructures for Sensing and Photocatalysis. Accounts of Chemical Research. 2022; 55: 831–843. https://doi.org/10.1021/acs.accounts.1c00682.

[17] Lee S, Hwang H, Lee W, Schebarchov D, Wy Y, Grand J, *et al*. Core–Shell Bimetallic Nanoparticle Trimers for Efficient Light-to-Chemical Energy Conversion. ACS Energy Letters. 2020; 5: 3881–3890. https://doi.org/10.1021/acsenergylett.0c02110.

[18] Stankevičius E, Ignatjev I, Petrikaitė V, Selskis A, Niaura G. Gold Nanoparticles Generated Using the Nanosecond Laser Treatment of Multilayer Films and Their Use for SERS Applications. ACS Omega. 2021; 6: 33889–33898. https://doi.org/10.1021/acsomega.1c05165.

[19] Zhang W, Tian Q, Chen Z, Zhao C, Chai H, Wu Q, *et al*. Arrayed nanopore silver thin films for surface-enhanced Raman scattering. RSC Advances. 2020; 10: 23908–23915. https://doi.org/10.1039/d0ra03803b.

[20] Charconnet M, Kuttner C, Plou J, García-Pomar JL, Mihi A, Liz-Marzán LM, *et al*. Mechanically Tunable Lattice-Plasmon Resonances by Templated Self-Assembled Superlattices for Multi-Wavelength Surface-Enhanced Raman Spectroscopy. Small Methods. 2021; 5: e2100453. https://doi.org/10.1002/smtd.202100453.

[21] Chen F, Zhao Y, Zhang S, Wei S, Ming A, Mao C. Hydrophobic Wafer-Scale High-Reproducibility SERS Sensor Based on Silicon Nanorods Arrays Decorated with Au Nanoparticles for Pesticide Residue Detection. Biosensors. 2022; 12: 273. https://doi.org/10.3390/bios12050273.

[22] Wang K, Li J. Reliable SERS detection of pesticides with a large-scale self-assembled Au@4-MBA@Ag nanoparticle array. Spectrochimica Acta. Part A, Molecular and Biomolecular Spectroscopy. 2021; 263: 120218. https://doi.org/10.1016/j.saa.2021.120218.

[23] Fu BB, Tian XD, Song JJ, Wen BY, Zhang YJ, Fang PP, *et al*. Self-Calibration 3D Hybrid SERS Substrate and Its Application in Quantitative Analysis. Analytical Chemistry. 2022; 94: 9578–9585. https://doi.org/10.1021/acs.analchem.2c00436.

[24] Wu Y, Yu Q, Joung Y, Jeon CS, Lee S, Pyun SH, *et al*. Highly Uniform Self-Assembly of Gold Nanoparticles by Butanol-Induced Dehydration and Its SERS Applications in SARS-CoV-2 Detection. Analytical Chemistry. 2023; 95: 12710–12718. https://doi.org/10.1021/acs.analchem.3c01348.

[25] Fang G, Hasi W, Sha X, Cao G, Han S, Wu J, *et al*. Interfacial Self-Assembly of Surfactant-Free Au Nanoparticles as a Clean Surface-Enhanced Raman Scattering Substrate for Quantitative Detection of As^{5+} in Combination with Convolutional Neural Networks. The Journal of Physical Chemistry Letters. 2023; 14: 7290–7298. https://doi.org/10.1021/acs.jpclett.3c01969.

[26] Hanske C, Hill EH, Vila-Liarte D, González-Rubio G, Matricardi C, Mihi A, *et al*. Solvent-Assisted Self-Assembly of Gold Nanorods into Hierarchically Organized Plasmonic Mesostructures. ACS Applied Materials & Interfaces. 2019; 11: 11763–11771. https://doi.org/10.1021/acsami.9b00334.

[27] Xing C, Zhong S, Liu D, Zhang T, Cao A, Zeng P, *et al*. Hydrogel Film@Au Nanoparticle Arrays Based on Self-Assembly Co-Assisted by Electrostatic Attraction and Hydrogel-Shrinkage for SERS Detection with Active Gaps. Advanced Materials Interfaces. 2021; 8: 2101055. https://doi.org/10.1002/admi.202101055.

[28] Yu Y, Chen Z, He S, Zhang B, Li X, Yao M. Direct electron transfer of glucose oxidase and biosensing for glucose based on PDDA-capped gold nanoparticle modified graphene/multi-walled carbon nanotubes electrode. Biosensors & Bioelectronics. 2014; 52: 147–152. https://doi.org/10.1016/j.bios.2013.08.043.

[29] Wang R, Xu Y, Sors T, Irudayaraj J, Ren W, Wang R. Impedimetric detection of bacteria by using a microfluidic chip and silver nanoparticle based signal enhancement. Mikrochimica Acta. 2018; 185: 184. https://doi.org/10.1007/s00604-017-2645-x.

[30] Sennakesavan G, Mostakhdemin M, Dkhar LK, Seyfoddin A, Fatihhi SJ. Acrylic acid/acrylamide based hydrogels and its properties - A review. Polymer Degradation and Stability. 2020; 180: 109308. https://doi.org/10.1016/j.polymdegradstab.2020.109308.

[31] Celestino GG, Henriques RR, Shiguihara AL, Constantino VRL, de Siqueira Melo R, Amim Júnior J. Adsorption of gallic acid on nanoclay modified with poly(diallyldimethylammonium chloride). Environmental Science and Pollution Research International. 2019; 26: 28444–28454. https://doi.org/10.1007/s11356-018-3505-x.

[32] Mwangi IW, Ngila JC, Ndungu P, Msagati TAM. Method Development for the Determination of Diallyldimethylammonium Chloride at Trace Levels by Epoxidation Process. Water, Air, and Soil Pollution. 2013; 224: 1638. https://doi.org/10.1007/s11270-013-1638-6.

[33] Li S, Yang F, Xiang K, Chen J, Zhang Y, Wang J, *et al*. A Multifunctional Microspheric Soil Conditioner Based on Chitosan-Grafted Poly(acrylamide-*co*-acrylic acid)/Biochar. Langmuir: the ACS Journal of Surfaces and Colloids. 2022; 38: 5717–5729. https://doi.org/10.1021/acs.langmuir.2c00317.

[34] Sivaselvam S, Selvakumar R, Viswanathan C, Ponpandian N. Rapid one-pot synthesis of PAM-GO-Ag nanocomposite hydrogel by gamma-ray irradiation for remediation of environment pollutants and pathogen inactivation. Chemosphere. 2021; 275: 130061. https://doi.org/10.1016/j.chemosphere.2021.130061.

[35] Madadi A, Wei J. Characterization of Calcium Silicate Hydrate Gels with Different Calcium to Silica Ratios and Polymer Modifications. Gels (Basel, Switzerland). 2022; 8: 75. https://doi.or

g/10.3390/gels8020075.

[36] Prusty K, Swain SK. Nano silver decorated polyacrylamide/dextran nanohydrogels hybrid composites for drug delivery applications. Materials Science & Engineering. C, Materials for Biological Applications. 2018; 85: 130–141. https://doi.org/10.1016/j.msec.2017.11.028.

[37] Zheng M, Cai K, Chen M, Zhu Y, Zhang L, Zheng B. pH–responsive poly(gellan gum–co–acrylamide–co–acrylic acid) hydrogel: Synthesis, and its application for organic dye removal. International Journal of Biological Macromolecules. 2020; 153: 573–582. https://doi.org/10.1016/j.ijbiomac.2020.03.024.

[38] Matouk Z, Islam M, Gutiérrez M, Pireaux JJ, Achour A. X-ray Photoelectron Spectroscopy (XPS) Analysis of Ultrafine Au Nanoparticles Supported over Reactively Sputtered TiO_2 Films. Nanomaterials (Basel, Switzerland). 2022; 12: 3692. https://doi.org/10.3390/nano12203692.

[39] Dong J, Yuan J, Cao Y, Zhao Y, Han Q, Gao W, *et al*. Electrically controllable self-assembly of gold nanorods into a plasmonic nanostructure for highly efficiency SERS. Optics Letters. 2022; 47: 6365–6368. https://doi.org/10.1364/OL.477507.

[40] Gates BD, Xu Q, Stewart M, Ryan D, Willson CG, Whitesides GM. New approaches to nanofabrication: molding, printing, and other techniques. Chemical Reviews. 2005; 105: 1171–1196. https://doi.org/10.1021/cr030076o.

[41] Song K, Xue W, Li X, Chang Y, Liu M. Self-Assembly of Single-Virus SERS Hotspots for Highly Sensitive In Situ Detection of SARS-CoV-2 on Solid Surfaces. Analytical Chemistry. 2024; 96: 8830–8836. https://doi.org/10.1021/acs.analchem.4c01607.